PCCP

Structural Water in Amorphous Carbonate Minerals: Ab Initio Molecular Dynamics Simulations of X-ray Pair Distribution Experiments

Journal:	*Physical Chemistry Chemical Physics*
Manuscript ID	CP-ART-10-2022-004881.R2
Article Type:	Paper
Date Submitted by the Author:	13-Jan-2023
Complete List of Authors:	Prange, Micah; Pacific Northwest National Laboratory Mergelsberg, Sebastian; Pacific Northwest National Laboratory Kerisit , Sebastien ; Pacific Northwest National Laboratory,

ARTICLE

Structural Water in Amorphous Carbonate Minerals: Ab Initio Molecular Dynamics Simulations of X-ray Pair Distribution Experiments

Received 00th January 20xx,
Accepted 00th January 20xx

DOI: 10.1039/x0xx00000x

Micah P. Prange,[a] Sebastian T. Mergelsberg[a] and Sebastien N. Kerisit*[a]

Water is known to play a controlling role in directing mineralization pathways and stabilizing metastable amorphous intermediates in hydrous carbonate mineral $MCO_3 \cdot nH_2O$ systems, where M^{2+} is a divalent metal cation. Despite this recognition, the nature of the controls on crystallization are poorly understood, largely owing to the difficulty in characterizing the dynamically disordered structures of amorphous intermediates at the atomic scale. Here, we present a series of atomistic models, derived from ab initio molecular dynamics simulation, across a range of experimentally relevant cations (M=Ca, Mg, Sr) and hydration levels ($0 \leq n \leq 2$). Theoretical simulations of the dependence of the X-ray pair distribution function on the hydration level *n* show good agreement with available experimental data and thus provide further evidence for a lack of significant nanoscale structure in amorphous carbonates. Upon dehydration, the metal coordination number does not change significantly, but the relative extent of water dissociation increases, indicating that a thermodynamic driving force exists for water dissociation to accompany dehydration. Mg strongly favors monodentate conformation of carbonate ligands and shows a marked preference to exchange monodentate carbonate O for water O upon hydration, whereas Ca and Sr exchange mono- and bidentate carbonate ligands with comparable frequency. Water forms an extensive hydrogen bond network among both water and carbonate groups that exhibits frequent proton transfers for all three cations considered suggesting that proton mobility is likely predominantly due to water dissociation and proton transfer reactions rather than molecular water diffusion.

INTRODUCTION

In addition to obvious fundamental questions in aquatic[1] and terrestrial[2-4] (bio)geochemistry, there is a critical need to understand carbonate phase transformation processes and their fundamental limits to envision and evaluate long-term carbon sequestration strategies based on mineralization[5] or utilization of carbonate-based materials.[6, 7] Divalent cations like Mg^{2+}, Ca^{2+}, and Sr^{2+} can be stabilized to varying degrees in a complicated manifold of hydrated solid phases, many of which are difficult to study because they are transient and disordered, appearing as intermediate phases in transformations that ultimately convert dissolved reactants to thermodynamically stable crystalline products. Water is understood to play an important role in modulating the relative stabilities and thermodynamic barriers that control the time dependent phase behavior of carbonate intermediates along this pathway.[8-10] To link the solution state chemistry of carbon to its incorporation in persistent solids, therefore, requires knowledge regarding the structural arrangement of water in metastable, poorly ordered carbonate solids, which are the focus of this work.

A structural model of amorphous calcium carbonate (ACC) consisting of a calcium-rich framework with nanopores containing water and carbonate molecules was put forward based on a reverse Monte Carlo (MC) refinement of X-ray total scattering data.[11] However, subsequent classical molecular dynamics (CMD) simulations that used this structural model as starting point predicted significant structural reorganization,[12] and other structural models, including our ab initio molecular dynamics (AIMD) simulations,[13] showed that good agreement with neutron and X-ray pair distribution function (PDF) analyses could be obtained with homogeneous models. This example highlights the fact that measurements such as X-ray total scattering, which are key to probing the short-range structure of amorphous carbonates, are dependent on structural models for accurate interpretation. Therefore, this work employs AIMD simulations based on density functional theory (DFT) to produce structural models from first principles.

Beyond structure, information regarding the chemical and dynamical state of water is needed to facilitate the elucidation of precipitation and transformation processes. Proton nuclear magnetic resonance (NMR) measurements by Michel et al.[14] suggested the presence of three water species in hydrated ACC: mobile molecular water (~55%), rigid molecular water (~40%), and hydroxide ions (~7%). The same measurements as a function of water content in ACC indicated that the absolute hydroxide content remained approximately constant as ACC dehydrated while the rigid and mobile water populations

[a] *Physical and Computational Sciences Directorate, Pacific Northwest National Laboratory, Richland, Washington 99352, United States.*
**Email: sebastien.kerisit@pnnl.gov*

Electronic Supplementary Information (ESI) available: [details of any supplementary information available should be included here]. See DOI: 10.1039/x0xx00000x

decreased to a similar extent upon dehydration.[15] The rigid molecular water population was inferred to be coordinated to Ca cations, but CMD simulations indicated that the fraction of diffusing water molecules was small (~2%),[16] and empirical potential structural refinement (EPSR) of X-ray and neutron total scattering data concluded that 90% of water molecules were coordinated to Ca cations.[17] Again, matching experimental measurements to the short-range structure of amorphous carbonates is very challenging, and, while much attention has been focused on elucidating the structural and dynamical properties of water in ACC, a consistent atomic-level picture is still lacking.

Meanwhile, data on structural water in amorphous carbonates other than ACC is comparatively limited. Leukel et al.[18] showed from Fourier transform infrared spectroscopy (FTIR) and ^{1}H NMR spectroscopy that hydrogen bonding was much weaker in ACC than in amorphous magnesium carbonate (AMC) and amorphous strontium carbonate (ASC). Atomistic simulations of these three amorphous carbonates, as a function of water content, would thus be beneficial to help understand how the nature of the divalent cation influences water structure in amorphous carbonates. Therefore, whereas our previous work focused on ACC at a single hydration level,[13] this work aims to facilitate insight into the relationship between the hydration level and the atomic-scale bonding motifs in amorphous carbonates by providing ensembles of ab initio structural models describing the variation of short- and medium-range (0–8 Å) atomic arrangements of hydrated AMC, ACC, and ASC across a range of hydration levels. The methods employed here derive the interatomic forces from electronic structure treated at the DFT level and hence include chemical reactivity. This ab initio approach avoids the difficulties of parameterizing transferable interatomic potentials and yields trajectories (i.e., dynamic structures) that obey both quantum and classical mechanical microscopic physics. We compare the computational results with available data from the literature and discuss the implications for unravelling the complex phenomena involved when carbonate materials precipitate.

METHODS

Density functional theory calculations

As in past work,[13, 19-22] we used DFT performed with VASP (Vienna Ab-initio Simulation Package)[23, 24] using the Perdew, Burke, and Ernzerhof[25, 26] (PBE) exchange-correlation functional augmented by the Grimme dispersion corrections (D3).[25, 26] PBE-D3 yielded the best agreement (Table S1) with the measured lattice parameters of the three carbonate minerals used as benchmark (aragonite, calcite, and monohydrocalcite, Fig. 1) of the eight exchange-correlation functionals (PBE, RPBE,[27] revPBE,[28] and PBEsol[29] with and without D3 Grimme dispersion corrections) evaluated in this work. Core electrons were treated with the standard projector augmented-wave (PAW) approach.[30, 31] The PBE PAW potentials from the VASP database for H, C, O, Mg, Ca, and Sr were used. These remove 0, 2, 2, 4, 12, and 28 electrons from the DFT calculation for each element, respectively. AIMD simulations were performed in the NVT (constant number of particles, constant volume, and constant temperature) and NPT (constant pressure) ensembles with an integration time step of 0.5 fs and at the Γ point (1 × 1 × 1 *k*-point mesh). The temperature was fixed by a Nosé-Hoover thermostat[32, 33] with the fictitious mass set to 3.0 for NVT runs. In NPT calculations, a Langevin thermostat[34, 35] with damping coefficient of 10 ps^{-1} was used for all degrees of freedom. The convergence criterion for the electronic self-consistent calculation was 10^{-5} eV throughout.

Amorphous structural model ensemble generation

We extended our previous work[13] at *n*=1 to different hydration levels using the same approximations. We briefly describe the strategy here for completeness. Our calculations were performed in (initially) cubic boxes with 24 (*n*=0, 0.5, 1) or 18 (*n*=1.5, 2) each of CO_3^{2-} carbonate groups and M^{2+} (M=Mg, Ca, Sr) metal cations and an appropriate number of water molecules. Initial amorphous configurations were generated by randomly placing the molecular groups on a cubic grid followed by relaxation and equilibration for 1 ns at room temperature with CMD using DL_POLY Classic.[36] Simulation parameters for these calculations were the same as in our previous work.[13] The potential parameters for water were those of the flexible SPC model[37] and the parameters for magnesium, calcium, and strontium carbonate were those used by de Leeuw and Parker,[38] Kerisit and Parker,[39] and de Leeuw,[40] respectively. DFT energy minimizations of the appropriate cation in the calcite (Mg and Ca) or aragonite (Sr) (MCO_3), monohydrocalcite ($MCO_3{\cdot}H_2O$),[41] and ikaite ($MCO_3{\cdot}6H_2O$) structures were performed, and quadratic regressions to the resulting densities as a function of water content were used to determine the initial size of the cubic box at each hydration level for each cation. With the volume held constant, these initial CMD structures were melted in AIMD at T=1500 K and, starting at 16 ps, a configuration was drawn for the quench stage at 9 ps intervals for a total of six starting molten configurations. The dynamics of the melted systems (residence time correlation functions (Fig. S1), half-life values of the first coordination shell of the divalent cations (Table S2), mean square displacement functions (Fig. S2), and diffusion coefficients of Mg, Sr, Ca, C, and O (Table S3)) shows that, as was demonstrated for ACC with *n* = 1 in our previous work,[13] the melting temperature and melting time were sufficient to ensure the six starting molten configurations were not correlated regardless of the divalent cation or the hydration level. The molten configurations, which were prepared using a lower 300-eV energy cutoff, were quenched to room temperature (300 K) at a rate of 300 K/ps to generate models of the hydrated, amorphous solids. These quenched configurations were then run in the NVT ensemble for 12 ps using a 600-eV energy cutoff to accumulate 960 snapshots by sampling the structure every 12.5 fs. Subsequently, the final structures of the NVT simulations were used as starting points for 12-ps NPT simulations from which another set of 960 snapshots were collected. The relaxation of the cell parameters constitutes a theoretical estimate of the system density. A simulation time of 12 ps was sufficient to approximate a normal distribution of the system volume and thus compute a mean density. The standard deviation of the

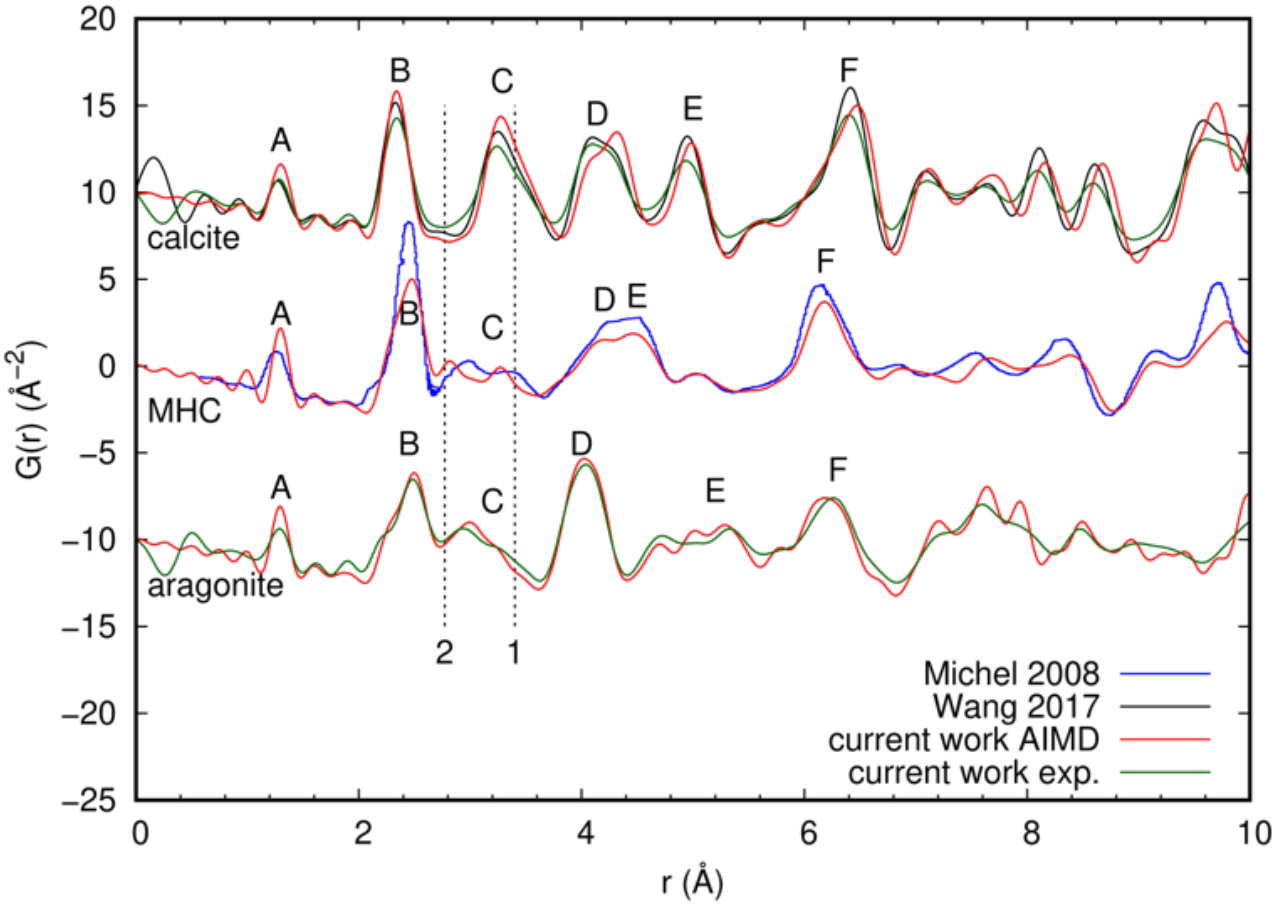

Figure 1: Theoretical (red) and experimental (other colors) X-ray PDF data of calcite, monohydrocalcite, and aragonite. The experimental data were measured by Wang et al.[49], (calcite), Michel et al.[14] (monohydrocalcite), and as part of this work (aragonite and calcite). The dotted lines labeled 1 and 2 (at r=3.40 and 2.77 Å, respectively) are reproduced in Fig. 3b below and bound the crystallographic Ca-C distances associated with mono- (1) and bi-dentate (2) Ca–CO_3 conformations.

density distribution for an example case (ACC with n =1) was 0.02 g/cm^3 (Fig. S3). Thus, each composition was represented by an ensemble over both configurational and thermal fluctuations. Below we present results obtained by averaging the six NPT AIMD simulations performed for each cation, except where noted otherwise.

PDF simulation

To simulate PDF measurements, we used the DISCUS package[42] to calculate the X-ray scattering intensity followed by Fourier transformation (FT) to real-space to produce $G(r)$. The transformation from Q to r space is affected by several numerical parameters that reflect the finite resolution and geometry of the experimental setup and are described in detail in the DISCUS documentation. Importantly, the finite upper limit of the FT integral introduces visible truncation ripples[43, 44] in the resulting $G(r)$ that can interfere constructively or destructively with the PDF, affecting the physical interpretation. To produce a consistent set of comparable calculations and compare with a range of experiments, we set Q_{damp}=0.01 Å^{-1}, Q_{broad}=0 and Q_{max}=19 Å^{-1}. The first two of these values reflect the finite resolution of the detector. Since we average over many frames of AIMD trajectory, the results we obtain do not depend on the values of Q_{damp} or Q_{broad} since the peak width is dominated by thermal broadening. As commented above, the simulated PDF does change with Q_{max} if the scattered (diffracted) intensity remains finite at Q=Q_{max}; the value we used was chosen as a typical reported value. We did not include any corrections for particle shape or size.

PDF experiments

To determine the PDF of crystalline standard materials, we performed total X-ray scattering at beam line 11-ID-B of the Advanced Photon Source (APS) at Argonne National Laboratory (Lemont, IL).[45] Sample powders were measured in 0.8 mm inner diameter (ID) Kapton capillaries. An amorphous silicon-based area detector (2048 × 2048 pixel Perkin-Elmer)[46] was positioned approximately 16 cm from the samples to collect the 2D total X-ray scattering data. The energy of the X-ray beam was a constant 58.66 keV (λ = 0.2114 Å) and a cerium dioxide calibrant (CeO_2, NIST diffraction intensity standard set 674a) diluted with glassy carbon (ratio 1:25 CeO_2 to carbon) was used to calibrate sample-to-detector distance and the detector tilt and rotation. For the samples and the empty capillary background, 60 frames of 1 second exposures were summed together and integrated from 2D to 1D using GSAS-II.[47] Background subtraction, sample normalization, and computation of $S(q)$, $F(q)$, and $G(r)$ were completed using PDFgetX2.[48]

RESULTS AND DISCUSSION

Methods benchmark: crystalline calcium carbonates

To understand the role that structural water plays, and to benchmark the simulation methods employed in this work, we compared simulated and measured X-ray PDFs of monohydrocalcite (MHC: $CaCO_3{\cdot}H_2O$) (Fig. 1) with the anhydrous calcium carbonate polymorphs calcite (the same simulation we reported in Prange et al.[28] as the bottom trace of Fig. 1) and aragonite. The experimental data came from our own measurements (aragonite and calcite) or from Wang et al.[49] (calcite) and Michel et al.[14] (MHC). The overall agreement is excellent, exhibiting a clear one-to-one correspondence between features and semiquantitative agreement in the absolute value of the PDF. This agreement imparts confidence that the computational (this work) and experimental (this work and Refs. [14, 49]) methods capture the PDF signal with sufficient fidelity to be usefully compared. This agreement also allows for confident assignment of the peaks. The peak labels in Fig. 1 have the following rough correspondences: A (intra-carbonate O–C), B (Ca–O and intra-carbonate O–O), C (Ca–C and inter-carbonate distances), and D-F (Ca–Ca and miscellaneous). We highlight the region 2.5 Å $\leq r \leq$ 4 Å, which contains Ca–C distances associated with CO_3^{2-} groups with an O atom in the first coordination shell of Ca^{2+} as well as intermolecular O–O distances. In our earlier analysis of ACC PDF[13] we found this region in *r* gave rise to the most significant disagreement between available atomistic models and the measured PDF. The materials in Fig. 1 display exclusively monodentate (calcite) and evenly mixed mono- and bidentate (MHC and aragonite) conformations of Ca^{2+} by CO_3^{2-} groups. The unique Ca-C distance (3.21 Å) in calcite corresponds to peak C, which is prominent in that system, and falls in the range 3.16-3.4 Å of Ca-C distances associated with monodentate configurations in these crystals. The bidentate configurations yield Ca-C distances from 2.77 Å (MHC) to 2.94 Å (aragonite). The maximum and minimum of this range are marked in dotted lines in Fig. 1. There is a clear shift of PDF intensity to shorter distances with increasing bidentate prevalence, although the analysis is complicated by the differing hydration levels.

The slight mismatches in the position of the peaks near the label 'C' and the intensity of the Ca–O first shell peak 'B' in the MHC PDF are intriguing. The peak positions in the PDF derived from the AIMD simulations agree with those in (static) simulations of the PDF from published structures determined by X-ray diffraction (XRD).[41] This is not surprising since our AIMD simulations used the XRD structure as a starting point, and DFT relaxations starting from the XRD structure yield very similar structural parameters. Michel et al. reported small amounts of aragonite or calcite in the MHC sample, which could explain the low-*r* shoulder of 'A' present in the Michel data but not the intensity disagreement regarding peak 'B'. This peak appears anomalously strong compared to the calcite, aragonite, and vaterite samples compared in Fig. 5 of Ref. [14]. Another possible explanation is that the carbonate groups, which contribute O–O distances at the low-*r* side of 'A' in MHC, might be distorted in a manner similar to those reported by Sen et al.[50] on the basis of NMR.

Amorphous carbonates: PDF

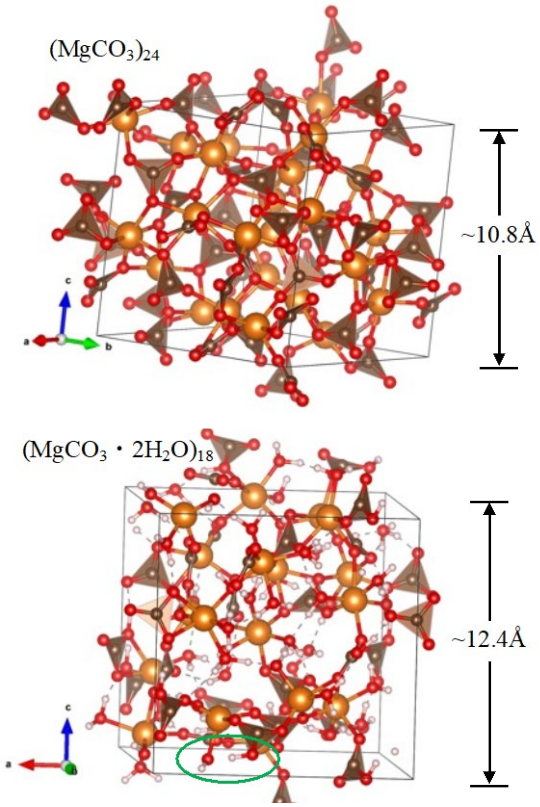

Figure 2: View (produced by VESTA[51]) of a structure visited in an AIMD simulation of a model AMC with *n*=0 (top) and *n*=2 (bottom). The green oval in the bottom panel marks a water molecule that has disassociated.

Amorphous models of Mg^{2+} (AMC), Ca^{2+} (ACC), and Sr^{2+} (ASC) carbonates were simulated at 5 hydration levels $0 \leq n \leq 2$. Two frames from the AIMD simulations of AMC are shown in Fig. 2 as illustrations. One snapshot per divalent cation-hydration level combination is presented in Fig. S4 through Fig. S6. Fig. 3 presents the PDF and the change induced in the PDF per unit increase in hydration level *n* for the three cations compared to published PDFs where available. Vertical dotted lines are included in Fig. 3 at the sum of the metal and O ionic radii,[52] which closely matches the observed M–O peak in the PDFs and serves as a length scale to aid interpretation of the features in the difference curves plotted below the PDFs. Also included in Fig. 3 are labels for the peaks A, B, D, and F from Fig. 1 to aid comparison between amorphous and ordered systems. Comparisons to the published data have been made by carefully tabulating published PDF curves from studies that varied the hydration level in AMC[17, 53, 54] and ACC[15] and taking differences of them. The ACC simulation was performed with Q_{max}=22 Å^{-1}. Jensen et al.[17] also measured ACC with multiple hydration levels just as for the AMC data shown in Fig. 3a (blue curves), but we have not included this data in Fig. 3 due to difficulties that we attribute to different normalizations of the data at different hydration levels, which complicates extraction of the difference signal (we attribute the oscillations in the difference signal in the AMC data of Yamamoto et al.[53] similarly to normalization issues). Albéric et al.[55] presented PDF data for ACC as it was dehydrated by heating in the range 1.4>*n*>0.4 that we did not include in Fig. 3 because we were not able to successfully

extract the PDF curves from the publication figures. Their data (e.g. Figs. 1 and S4 of Ref. [55]) appear to be in qualitative agreement with our results and those published by Schmidt et al.[15] and Jensen et al.[17] The studies of AMC by Jensen et al.[17, 54] and Yamamoto et al.[53] are the only ones we are aware of that include PDF data at multiple hydration levels. We have cut off the experimental difference curves in Fig. 3a at low *r* for clarity, since the reported PDFs in this region are far below the simulated ones by an amount that varies between the hydration levels (c.f. the top curves in Fig. 3a near peak A ~1.3 Å). We are unaware of any hydration dependent data for ASC. This lack of hydration-dependent ASC data is likely due to the difficulty of stabilizing the amorphous structure against crystallization.[56, 57] Hence, for ASC, we include the Leukel et al. measurement[57] at a single hydration level. We acknowledge there are significant uncertainties in these comparisons arising from differences in material synthesis, PDF data collection and reduction, data presentation in the publications, and our collection and manipulation of those data. Reliable determination of the hydration levels, in particular, is a difficult problem. Still, we believe the comparisons can be useful for understanding how hydration affects the structure of amorphous carbonates and how these changes are reflected in the PDF experiments.

The agreement between the simulated PDF and experimental data is good at a qualitative level. Unsurprisingly, the level of agreement is not as high as for the crystalline materials considered above, but there is still a clear one-to-one correspondence between features in the simulated and measured PDF curves, and there are disagreements among the experimentally measured curves that are as large as those between simulated and measured curves. Since simulated and measured PDFs match well for crystalline materials and there is a lower level of reproducibility among experimental PDFs of amorphous systems, we conclude that the amorphous systems exhibit structural variation from sample to sample (i.e., the structure depends on synthesis procedures), consistent with observations from electron microscopy.[58] We note that the kind of analysis attempted here would be enhanced by a greater availability of experimentally measured PDFs, and we encourage the publication of new data, even for systems for which there is existing PDF data, along with careful reporting of the synthesis procedures used to produce the samples. Of the cations considered here, Ca^{2+} is the most intensively studied, and, as shown in Fig. 3, we also obtain the best agreement for this case. We discuss the three materials separately now.

AMC. The biggest change in the PDF of AMC upon increasing hydration level is the broadening of peak B, which causes the central region of the peak around the mean Mg-O first shell distance to lose intensity, mostly to the large *r* flank. As shown in Fig. 3, the general shape of the calculated changes upon hydration matches the experimental ones up to about 3 Å, but the prominent dip occurs at smaller *r* in the experiments than the simulations. The small ionic radius of Mg^{2+} causes the main Mg–O contributions (peak B) to appear before the intermolecular O–O distances (the Mg-O and O-O portions of peak B are potentially resolvable if $\boldsymbol{Q_{max} \geq 26\ \text{Å}^{-1}}$). Hence,

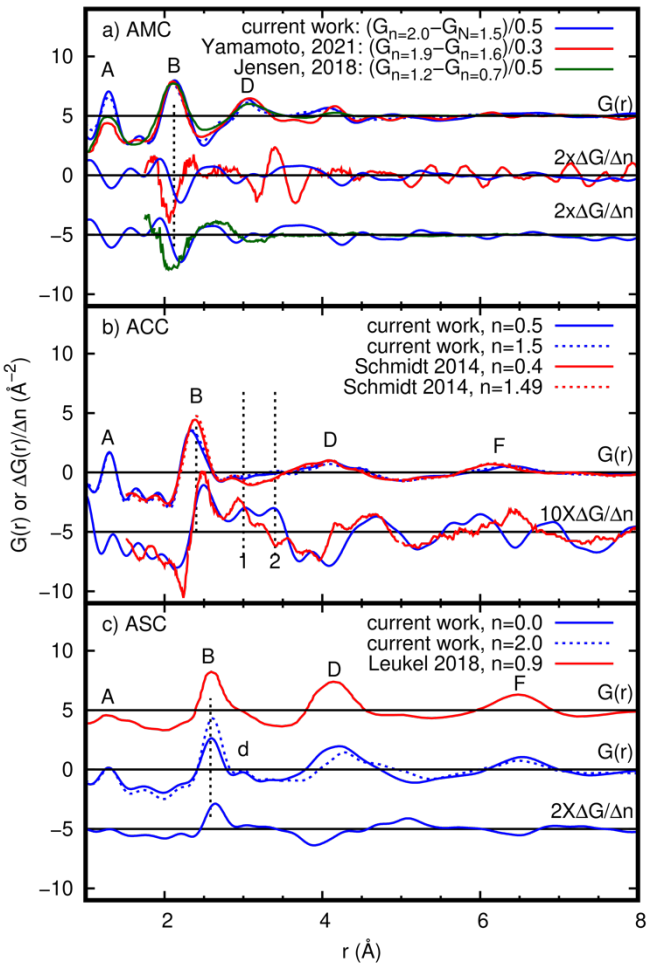

Figure 3: Comparison of calculated and measured PDFs of amorphous carbonates.

a: Simulated (blue) and measured (red, Yamamoto et al.[53] and green, Jensen et al.[17]) PDF of hydrated AMC. The top curves are the PDF (*n*=1.9 for Yamamoto et al. and *n*=1.2 for Jensen et al.), and the bottom two sets of curves show the difference between the more hydrated and less hydrated systems, normalized by the change in hydration levels. The simulated PDF is plotted for *n*=0 (solid) and *n*=1.5 (dotted).

b: Simulated (blue) and measured (red, Schmidt et al.[15]) PDF of ACC. The top curves are the PDF, and the bottom curves show the difference between the more hydrated and less hydrated systems, normalized by the change in hydration level and multiplied by 10 for clarity. The experimental data are those reported in Ref. [15] for synthesis method 1a initial material (*n*=1.49) and heated to 150 °C (*n*=0.4). The simulated PDFs are shown for *n*=0 (solid) and *n*=2 (dotted), simulated at Q_{max}=22 $Å^{-1}$ to match the experiment. Vertical dotted lines labelled 1 and 2 are the same as in Fig. 1 and mark features associated with bi- and monodentate CO_3–Ca conformations in crystalline calcium carbonates, respectively. No scaling was performed on the data in this panel.

c: Simulated (blue) and measured (red, Leukel et al. ,[57] offset vertically for clarity) PDF of ASC. The top two sets of curves are the PDF, and the bottom curve shows the difference between the simulated PDF for *n*=2 and *n*=0, normalized by the change in hydration level.

All simulated curves are from NPT simulations; vertical dotted lines are drawn at the sum of the Shannon ionic radii of O^{2-} and M^{2+}. Labels A, B, D, E mark features roughly corresponding to those in the crystalline calcium carbonate PDFs in Fig. 1.

features associated with O–H···O contribute to the low-*r* side of peak D instead of the high-*r* side of peak B as for the larger cations. This causes the high-*r* side of peak B peak to *decrease* with increasing hydration, in contrast to the larger cations. This

is due to normalization effects (the intra-carbonate O–O distances that contribute to this region constitute a smaller fraction of the interatomic distances) and a subtle lengthening of the average intra-carbonate O–O distance as the carbonate O atoms accept hydrogen bonds from water molecules. The intermolecular arrangements of C and Mg are also modified upon hydration in ways that are discernable in the PDF, leading to peaks in the difference curve in Fig. 3a at ~2.6 (between B and D) and ~3.7 Å (above D). The first is associated with a greater fractional prevalence of bidentate CO_3^{2-} groups (c.f. Fig. 4) as *n* increases, while the second is associated with a lengthening of Mg–Mg distances from ~3.2 Å to ~3.7 Å. In the anhydrous case, a common motif is a chaining of three Mg^{2+} ions in a linear fashion with a carbonate group possessing a bidentate interaction with the center Mg^{2+} and monodentate interactions with the flanking cations (see Fig. S7). When water is present in the structure, the flanking cations recede from the central cation, and water interactions replace the monodentate interactions with the 'original' carbonate group.

ACC. The trends in the simulated G(*r*) reproduce well those in the ACC data of Schmidt et al.[15] The main effect is an enhancement of the high-*r* side of peak B by O–H···O motifs. In the Ow–Oc radial distribution functions from the AIMD runs (Fig. S8), the O–H···O feature appears as a shoulder below *r*~3 Å. Peak D is shifted to higher *r* with increasing *n*, reflecting the larger Ca-Ca separation in the less dense material. The changes in the PDF arise from elongation of the distances involving C and O atoms that locally coordinate neighboring cations as well as the Ca-Ca distances themselves. This effect is reflected in the decrease in density of the AIMD models with hydration level, c.f. Table 1. We comment that agreement between the simulated and experimentally derived difference curves deteriorates as *r* is increased through the 'valley' region marked by the dotted lines labelled 1 and 2 between peaks B and D in Fig. 3b. As we noted in a previous paper,[13] this range in *r*, which contains many O-O and Ca-C distances, shows similar disagreement among several repeated theoretical[12, 13, 59] and experimental[14, 17, 49, 57] efforts. In this work, we see that this disagreement extends to the way the PDF changes with hydration level.

In an elegant experiment, Albéric et al.[55] studied the evolution of the PDF as ACC (initially $\boldsymbol{n} \approx 1.3$) was dehydrated by heating in an in situ XRD apparatus. They noted a shift in the peak we have labelled B (corresponding to the 'first derivative' lineshape in the experimental and theoretical difference curves in Fig. 3b) but did not offer any interpretation, except to note that the peak corresponds to the Ca-O first shell distance. With recourse to our atomistic models, we can attribute the apparent shift of the main Ca–O peak (B) to changes in the hydrogen bonding motifs instead of an actual shift in the Ca–O first shell distance. A similar comment applies to the Ca coordination number, which Albéric et al. could not determine by integration of the PDF because the density was unknown. Hence atomistic models can significantly extend insight into local structure by enabling interpretation of measured PDFs.

ASC. Among the cases considered here, the PDF of ASC undergoes the largest changes as the hydration level is raised from 0 to 2, making it the easiest to qualitatively analyze. The hydration of the ASC structure leads to two notable changes: peak B (~2.56 Å) is enhanced and shifted to slightly larger *r* and peak D at ~4 Å is shifted to higher *r*, similar to ACC. The changes in peak B are due to the addition of O–O distances involving hydrogen bonds donated by the water molecules (either to carbonate O atoms or to other water O atoms as we discussed above). The change in peak B is much more pronounced in ASC compared to ACC (see Fig. S8), which is consistent with the finding by Leukel et al. using ^{1}H NMR and FTIR spectroscopy that hydrogen bonding is stronger in ASC than ACC.[18] The shift in peak D is again present and more pronounced in ASC compared to ACC in our simulations for two reasons: 1) the metal-metal contribution to the PDF is enhanced by ~$(36/18)^2$=4 due to the larger X-ray scattering cross-section of Sr^{2+} compared to Ca^{2+}, and 2) the calculated density of ASC depends more strongly on hydration level than that of ACC. The O–O radial distribution functions in the intermolecular region evolve from a single asymmetric peak with maximum ~3.0 Å at *n*=0 to a double peak with distinct maxima at *r*=2.65 and 3.32 Å, corresponding to the presence of (O–H···O) and absence of a proton (and associated hydrogen bond) between the two O atoms, respectively. These shortest intermolecular O–O distances lead to the peak labeled 'd' in Fig. 3c (visible as a weak shoulder in the measurements of Leukel et al.[57]), but they do not produce any marked features in the difference curve (bottom curve of Fig. 3c) due to partial cancellation by changes to the Sr–O distances associated with the swelling of the material. As in AMC, we predict that the intra-carbonate O–O distances are resolvable as a separate peak if $\boldsymbol{Q_{max} \geq 26}$ Å^{-1}, but on the other (low-*r*) side of peak A.

Density of amorphous carbonates

Since the volume available for a given set of atoms constrains the possible chemical interactions among the atoms, the density (or molar volume) of amorphous carbonate materials (Table 1) is an important parameter for their simulation, with significant uncertainties in both experimental and theoretical determinations of the density leading to associated uncertainty in the simulated scattering signals, including PDF. To evaluate the ability of the current theoretical methods to reproduce the room temperature densities, we tabulate (Table 2) the theoretical AIMD densities for calcite, MHC, and aragonite obtained by analyzing the AIMD simulations that produced the PDF curves in Fig. 1.

ARTICLE

Table 1: Calculated densities, ρ (g/cm³), and excess molar volumes, ΔV (cm³/mol), of amorphous carbonates $MCO_3 \cdot nH_2O$. The reported uncertainties are the standard deviations obtained using the six mean densities calculated for each *M*/*n* combination, and the excess molar volumes are calculated with respect to liquid water and the appropriate anhydrous amorphous MCO_3·model.

M/*n*	**0**	**0.5**		**1**		**1.5**		**2**	
	ρ	**ρ**	**ΔV**	**ρ**	**ΔV**	**ρ**	**ΔV**	**ρ**	**ΔV**
Mg	2.61±0.03	2.37±0.04	-1.28	2.19±0.02	-1.83	2.03±0.03	-1.84	1.88±0.03	-1.47
Ca	2.62±0.03	2.46±0.03	-1.92	2.29±0.03	-2.37	2.20±0.03	-3.00	2.09±0.03	-3.08
Sr	3.51±0.04	3.21±0.04	-1.56	2.99±0.05	-2.13	2.76±0.04	-2.02	2.56±0.03	-2.18

Table 2: Densities (g/cm³) of calcium carbonate crystals.

Material	**NPT**	**Experiment**	**Percentage error**
Calcite	2.66±0.02	2.713[60]	−2.1%
Aragonite	2.84±0.03	2.92[61]	−2.4%
Monohydrocalcite	2.38±0.02	2.42[41]	−1.5%

Experimentally determined densities. Experimental determinations of the density of ACC fall in the range 2.4-1.6 g/cm³ and are collected here for comparison. Jensen et al.[17] measured the density of their synthetic hydrous ACC to be 2.282±0.002 and 2.428± 0.002 g/cm³ for *n*= 1.1 and 0.5, respectively, using Ar pycnometry. Cobourne et al.[62] reported a much less dense ACC (2.19 g/cm³ for *n*=0.25 using He pycnometry). Shuseki et al.[63] synthesized ACC with *n*=1 and reported a density of 2.1 g/cm³ (measured by pycnometry with unreported gas). Other estimates using small-angle X-ray scattering (SAXS)[64] and amplitude contrast analysis of transmission electron micrographs[65] have found very low values around 1.6 g/cm³. The density of samples can also be inferred indirectly from scattering experiments. Goodwin et al.[11] found good agreement for reverse MC structures fit to extended X-ray absorption fine-structure spectroscopy (EXAFS) data for *n*=1 ACC at the density of MHC (2.42 g/cm³).[41] Jensen et al.[66] used EPSR inversion of PDF data to infer the density of hydrated AMC: they report 1.92 and 1.93 g/cm³ for *n*=1.1 and 0.7, respectively.

Theoretically determined densities. The densities of the systems simulated in the current work using AIMD (Table 1) generally agree with previous computational estimates using CMD: Saharay et al.[67] calculated the density of ACC in the range $0 \leq \boldsymbol{n} \leq \mathbf{1}$, finding decreasing densities in the range 2.71-2.59 g/cm³ corresponding to 1%-7% more dense than the corresponding values from our AIMD simulations, while Bushuev et al.[59] reported excess molar volumes for *n*=1.0 also using CMD and melt-quench algorithms in agreement with the current work. For comparison, we have included excess molar volumes calculated with respect to liquid water (molar volume 18.07 cm³/mol[68]) and the *n*=0 simulation in Table 1. Malini et al.[69] compared different methods of generating starting structures in their CMD study of *n*=1.0 ACC and found 2.54-2.63 g/cm³.

Regarding the value of the density, we observe that theoretical models yield larger values than experimental ones, with the two ranges overlapping at their extrema. The current work, using AIMD, falls in this overlapping region. Regarding the dependence of the density on hydration level, we find a nearly linear trend in which the density decreases by approximately 0.33, 0.26, and 0.47 g/cm³ for each unit increase in the molar ratio H_2O:MCO_3 for M=Mg, Ca, Sr, respectively. The decrease in density from calcite to MHC is 0.29 g/cm³. From the experimental literature, we can infer the value of 0.25 g/cm³ from Jensen et al.[17] for ACC.

Hence, the density of hydrated amorphous carbonates is a key piece of missing scientific information that could significantly constrain theoretical models. By predicting the density using NPT melt-quench algorithms, we are implicitly simulating the precipitation process and assuming that the density of the solid is well reflected by the local minimum of the potential energy surface belonging to the basin of attraction of the parent molten state. Whether or why this procedure works is an important question in the simulation of amorphous structures.

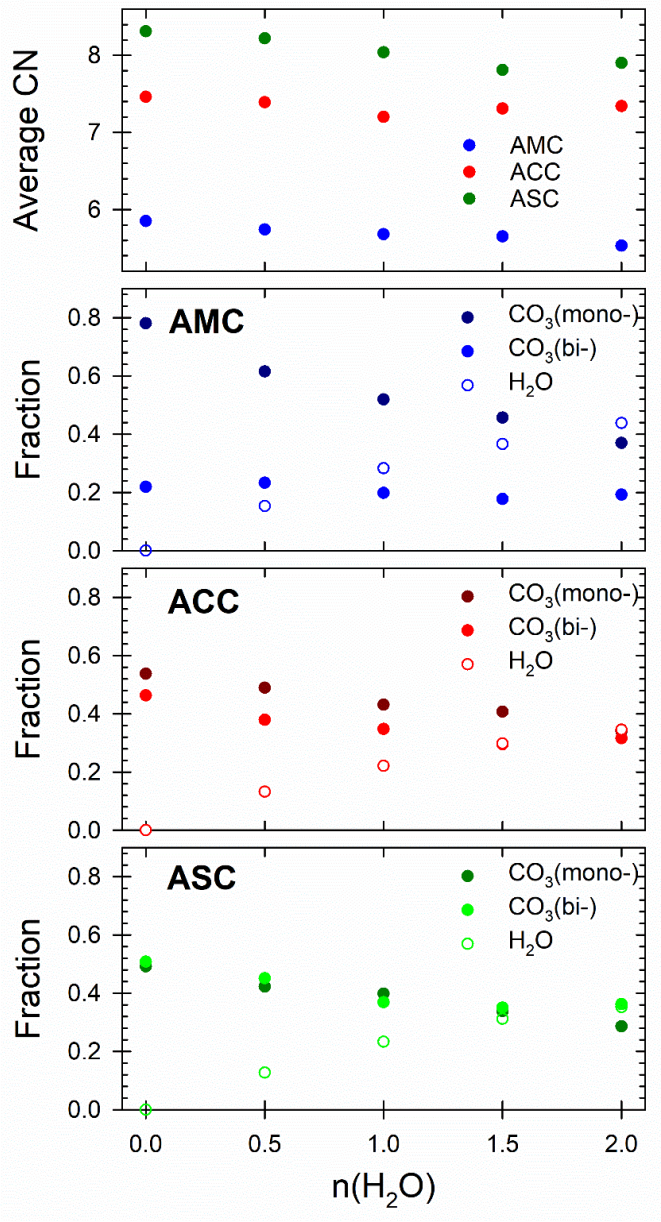

Figure 4: Average coordination numbers (CNs) of the cations in the models (top) and fractions of the coordinating O atoms that belong to water molecules or mono- or bidentate carbonate groups.

Metal ion coordination. Two primary types of bonding contribute to the energetic stability of hydrated carbonates: ionic metal–O interactions and hydrogen bonding mediated by the H_2O molecules. To probe the local cation environment, we computed coordination numbers (CNs) by integrating the metal–O RDFs (Fig. S9) up to the first minimum and classified the coordinating O atoms according to their speciation (H_2O or CO_3^{2-}). For the latter, we distinguished between and mono- and bidentate conformations. The averages of these populations are displayed in Fig. 4, while the distribution of instantaneous coordination numbers for each hydration level simulated is displayed in Fig. 5. A notable conclusion from this analysis is that CN does not vary strongly with *n*, and water mostly replaces carbonate O atoms instead of increasing the CN. In fact, there is a slight but consistent negative correlation

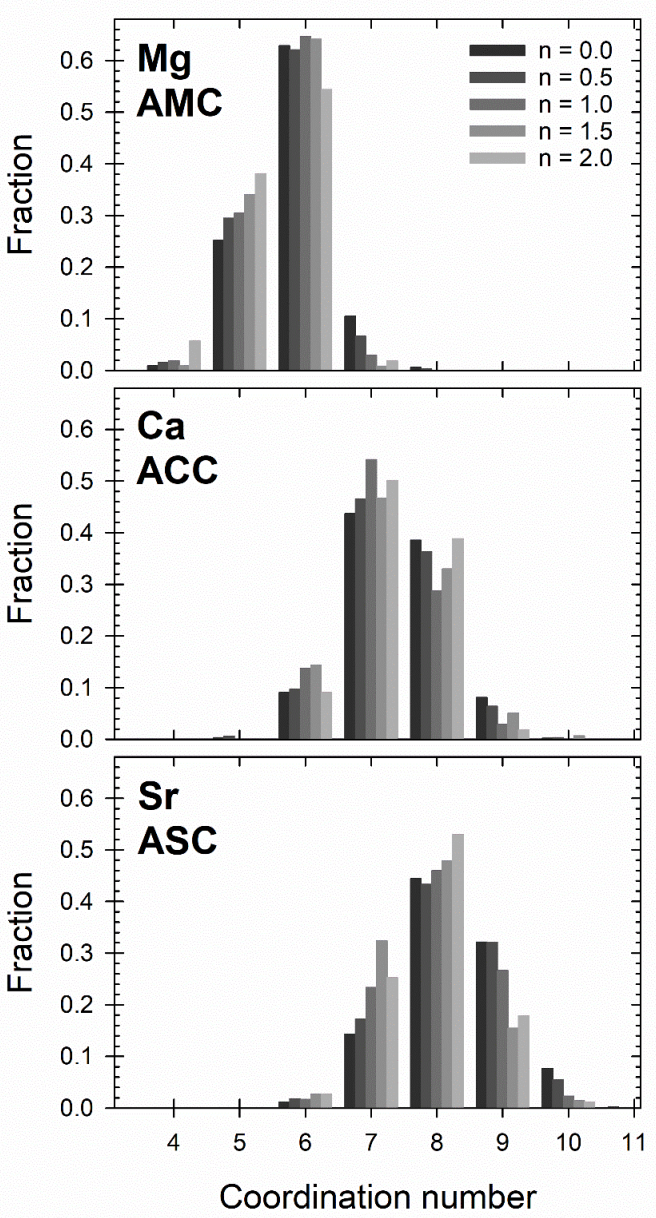

Figure 5: Coordination numbers of Mg (top), Ca (middle), and Sr (bottom) in the amorphous carbonate models at different levels of hydration.

between *n* and CN. The exchange of carbonate O for water O with hydration is different in AMC than ACC or ASC in that AMC shows a marked preference to exchange monodentate CO_3^{2-} conformations, while ACC and ASC exchange mono- and bidentate conformers with comparable frequency. This may be related to the width of the distribution (Fig. 5) of CNs (i.e., the flexibility of the different M^{2+} species to adopt different CNs). The maximum CN_{max} of the distribution occurs at 6, 7, and 8 for Mg^{2+}, Ca^{2+}, and Sr^{2+}, respectively, independent of *n*. Sr^{2+} displays flexibility and is found frequently in $CN_{max}\pm1$. On the other hand, Ca^{2+} shows a marked preference for $CN_{max}+1$, and Mg^{2+} is only rarely found with $CN_{max}+1$, especially for $n>0$. This suggests that ligand exchange must occur primarily through CN=5 intermediates during AMC precipitation and may be related to its propensity to retain bidentate CO_3^{2-} at large *n*.

Water dissociation. A significant advantage of the AIMD methods employed here relative to previous nonreactive classical MD models of amorphous carbonates is that chemical reactions can occur in AIMD. We do in fact observe proton transfers that dissociate water molecules producing hydroxide and bicarbonate species ($CO_3^{2-} + H_2O \rightleftharpoons HCO_3^- + OH^-$). This reaction occurs both in the T=1500 K melted and T=300 K quenched simulations, and has been observed in similar DFT work on AMC.[70] Fig. 6 shows the average extent of this reaction in the T=300 K production runs for the three cations as a function of *n*. There is the most dissociated water in AMC, and there is (fractionally) less water dissociation in more hydrated systems. The resulting OH^- groups facilitate further proton transfers with water. That AMC shows the most dissociated water can be attributed to the small radius and high ionic potential of Mg^{2+}, but Ca^{2+} does not show any significant increase over Sr^{2+}.

A study published by Leukel et al.[18] provides a good experimental comparison since the researchers synthesized all three amorphous carbonates studied here: AMC (n=0.8), ACC (n=0.4), and ASC (n=0.3), as well as amorphous Ba carbonate, and performed extensive characterization including FTIR and NMR, which can detect HCO_3^-. They found clear evidence for both OH^- and HCO_3^- (with more of the former than the latter) in their AMC samples, but not in ACC or ASC using a variety of NMR techniques (magic angle spinning ^1H, ^1H-^{13}C heteronuclear correlation, and $^{13}C\{^1H\}$ cross-polarization). They did not quantify the minor amounts of OH^- and HCO_3^- in AMC. HCO_3^- has also been occasionally reported in ACC. Huang et al.[71] also used heteronuclear correlation NMR to demonstrate the presence of HCO_3^- in synthetic ACC prepared at near-neutral pH (as opposed to the basic conditions typically employed). Other attempts at detecting bicarbonate ions in ACC have shown mixed results,[8, 14, 72, 73] so the incorporation or formation of HCO_3^- in ACC or other amorphous carbonates may be synthesis dependent. The existence of HCO_3^- in synthetic AMC and the observation of water dissociation on the time scales of AIMD simulation suggest that water dissociation may play a role in amorphous carbonate

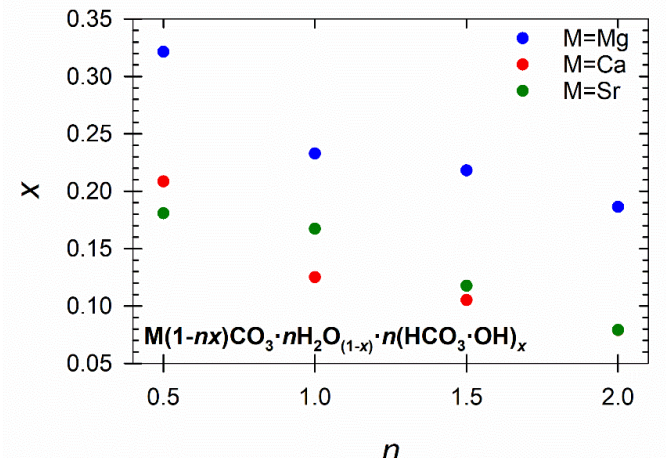

Figure 6: Mole fraction of water molecules that are dissociated in the amorphous structures.

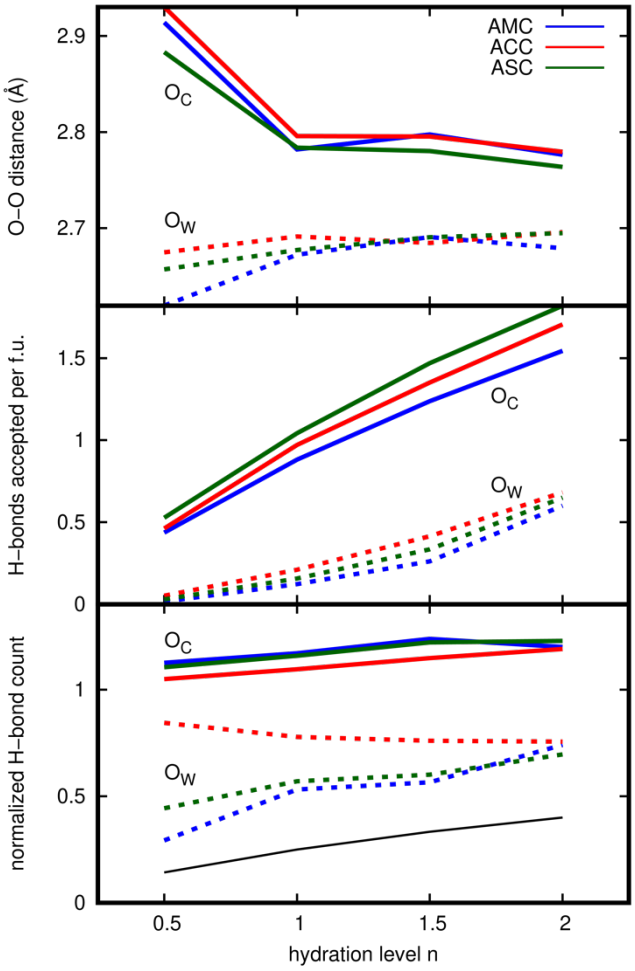

Figure 7: Average O–O distance in O–H··O, number of hydrogen bonds accepted by O type per $MCO_3{\cdot}nH_2O$ formula unit (middle), and the same quantity divided by the fraction of all oxygens that can accept hydrogen bonds of this type for O_C (solid lines) and O_W (dashed lines), all vs. *n*. If hydrogen bonding was uniformly distributed among possible acceptors, the corresponding plotted ratios would be 1 in the bottom panel; values greater than 1 indicate that the corresponding oxygen species receives more hydrogen bonds than if the bonds were distributed uniformly among O atoms that do not belong to the donating water molecule. The black line in the bottom panel marks the fraction of O atoms that are O_W vs. hydration level *n*.

chemistry. In this vein, we mention the quasielastic neutron scattering study of Jensen et. al.[74] that found significant proton mobility in AMC, but not in ACC. Their synthesized AMC, however, contained a significant population of OH^-, while their ACC did not contain detectable amounts of OH^-, so that proton transfer occurred in the AMC samples but not ACC. Even though Jensen et al. interpreted their results in terms of molecular water diffusion, our results suggest that water dissociation and proton transfer may be the main contributors to proton mobility.

We also point out that synthesis methods employing mechanochemical processes have been shown to produce HCO_3^- bearing ACC.[75] OH^-, on the other hand, is known to exist in ACC[74] and even more prominently in AMC,[18, 66] presumably either charge balanced by bicarbonate groups (as observed in our simulations) or a corresponding decrease in CO_3^{2-} (i.e., some fraction of $M(OH)_2$ phase). This formation of metal hydroxide cannot occur in our simulations due to the fixed stoichiometry of the models, and the relative prevalence of water dissociation in these models hints at the chemical stability of OH^- in amorphous carbonate structures (especially AMC). We plan future AIMD studies with metal/carbonate ratios greater than unity to explore this area.

Hydrogen bonding While it is now generally accepted that amorphous carbonates can be formed with a wide range of hydration levels, the nature of the hydrating water molecules is not well understood, particularly the role of hydrogen bonding in stabilizing amorphous structures. Several previous works have presented atomistic models of hydrated ACC[11, 12, 16, 17, 59, 62, 67, 76, 77] and AMC.[66, 70] We are not aware of any similar reports for ASC. To quantify the extent and strength of hydrogen bonding we plot the O-O distances in O–H··O motifs (top panel of Fig. 7) and the number of hydrogen bonds accepted by different O species (middle and bottom panels of Fig. 7) in two ways: the total number of hydrogen bonds per formula unit and the same quantity normalized by the relative frequency of carbonate (O_C) and water (O_W) oxygen atoms in the model. For this analysis, we counted O–H··O arrangements as hydrogen bonds according to the criteria proposed by Bylaska et al.:[78] O–O distance less than 3.2 Å and bond angle greater than 140°. We see that hydrogen bonding is extensive in these amorphous carbonate models (between 0.6 and 0.7 hydrogen bonds per H, similar to liquid water). This result is in agreement with Leukel et al.[18] (for AMC, ACC, and ASC) and Jensen et al.[17] (for ACC and AMC) and in disagreement with the CMD work of Saharay et al.[67] (for ACC). Also in line with the findings of Leukel et al.[18] is the relative strength of hydrogen bonding, which was inferred in that work from the location of the O–H stretch region in FTIR, yielding the ordering from strongest to weakest hydrogen bonds of ASC>AMC>ACC. We do not observe a strong trend in the O-O distances with cation type, but we do observe significantly longer O-O distances for hydrogen bonds to O_c compared to O_w.

There is a slightly greater number of hydrogen bonding for heavier cations (i.e., Sr > Ca > Mg). The suppression of hydrogen bonding in Mg^{2+} could be attributed to decreased structural flexibility stemming from the comparatively rigid quasi-octahedral first coordination shell, which might allow less local distortion to accommodate additional hydrogen bonds than larger and softer cations.

In our simulations, especially at low hydration levels, there is a marked preference for water molecules to form hydrogen bonds with CO_3^{2-} compared to H_2O, also in agreement with the findings of Jensen et al.[17] At higher hydration levels, it is more difficult to find carbonate sites for hydrogen bonding, and water–water hydrogen bonding becomes more prevalent, although it is dominated by water–carbonate hydrogen bonding even when normalized for the relative abundance of O_C (Fig. 7). The question of the partitioning of hydrogen bonds by acceptor (CO_3^{2-} or H_2O) is relevant because it is related to the existence or nonexistence of connected water clusters in amorphous carbonates. A series of studies using NMR[14, 15] and CMD combined with reverse MC fitting of X-ray scattering data[11] suggested that a significant amount of the incorporated water was mobile and not tightly bound to the ACC framework. Based on this evidence, the authors concluded that ACC consisted of nanoporous networks of mutually connected water molecules that allowed water mobility. The nanopores were not found in subsequent CMD[12] and EPSR[62] models, suggesting that homogenous disordered structures could account for all data, although recent work using EPSR and CMD has shown evidence for some degree of nanoporosity.[76, 77] To our knowledge, whether ACC (or other amorphous carbonates) feature connected channels is still an open question. But, like many other works,[55, 79] we find that open channels do not need to be invoked to reproduce PDF data. Conversely, the limited size of our AIMD models preclude them as a basis for ruling out the existence of such channels. Still the preponderance of evidence now seems to be in favor of homogeneous material lacking significant nanoscale structure.

Finally, we comment on an interesting cation effect that we observe in the partitioning of hydrogen bond acceptors in our simulations. As mentioned above, for $n \leq 1$, the water preferentially hydrogen bonds with CO_3^{2-} groups, and ASC exhibits the most hydrogen bonds of the materials studied here followed in order by Ca and Mg. The situation is different, however, if the analysis is restricted to the water–water hydrogen bonds. Here, Sr falls between Ca and Mg, reflecting relatively less propensity for water molecules to interact via hydrogen bonds in ASC.

Conclusions

We presented theoretical calculations of the hydration level dependence of the X-ray PDF signal in a series of amorphous carbonate minerals by taking ensemble averages over both

configurational and vibrational disorder. The structural ensembles were generated using a DFT-based AIMD melt-quench approach that has previously produced good agreement with neutron PDF, X-ray PDF, and EXAFS experiments of amorphous carbonates. We compared the current results with available experimental data, finding reasonable agreement. We analyzed the resulting structures in terms of metal coordination environment, proton transfer reactions, and hydrogen bonding, comparing to previous publications where feasible. This work adds to the substantial existing knowledge of water in ACC and extends this knowledge to the much less studied AMC and ASC systems. We conclude that the structure of AMC is significantly different from that of ACC and ASC in terms of metal coordination and extent of water dissociation. Additionally, the present work shows that metal coordination is mostly independent of hydration level, that extensive hydrogen bonding networks form as water is added to amorphous carbonate structures, and that this bonding is preferentially between the water molecules and carbonate groups. This work also demonstrates that the AIMD-derived structural models accurately predict the small changes in the X-ray PDFs of amorphous carbonates measured upon (de)hydration, which allows for extracting more information from measured PDFs than previously possible. This finding has implications for understanding and predicting carbonate transformation pathways because small differences in stoichiometry and structure of metastable intermediates may have a significant impact on the nature of the crystalline products. Finally, our models indicate that OH^- incorporation and water dissociation reactions can occur for all the materials studied and suggest that proton mobility is likely predominantly due to water dissociation and proton transfer reactions.

Author Contributions

MPP performed PDF simulations and analysis and wrote the paper. STM performed experiments and data analysis. SNK performed AIMD simulations and conceptualized the research.

Conflicts of interest

There are no conflicts to declare.

Acknowledgements

This work was supported by the U.S. Department of Energy (DOE), Office of Science, Office of Basic Energy Sciences, Chemical Sciences, Geosciences, and Biosciences Division through its Geosciences Program at Pacific Northwest National Laboratory (PNNL). PNNL is operated for DOE by Battelle Memorial Institute under Contract DE-AC05-76RL01830. The simulations were performed using PNNL Institutional Computing and the Environmental Molecular Sciences Laboratory (EMSL), a national scientific user facility sponsored by the U.S. DOE's Office of Biological and Environmental Research and located at PNNL in Richland, WA. This research used resources of the Advanced Photon Source, a U.S. DOE Office of Science User Facility operated for the DOE Office of Science by Argonne National Laboratory under Contract No. DE-AC0206CH11357. The authors also acknowledge Dr. Eric Bylaska for use of his hydrogen bond analysis code and Dr. Anne Chaka for useful discussions.

Notes and references

1. Y. U. T. Gong, C. E. Killian, I. C. Olson, N. P. Appathurai, A. L. Amasino, M. C. Martin, L. J. Holt, F. H. Wilt and P. U. P. A. Gilbert, *Proceedings of the National Academy of Sciences*, 2012, **109**, 6088-6093.
2. T. Plank and C. E. Manning, *Nature*, 2019, **574**, 343-352.
3. S. Farsang, M. Louvel, C. Zhao, M. Mezouar, A. D. Rosa, R. N. Widmer, X. Feng, J. Liu and S. A. T. Redfern, *Nature Communications*, 2021, **12**, 4311.
4. Q. Wang, Z. Zou, H. Wang, W. Wang and Z. Fu, *Journal of Colloid and Interface Science*, 2022, **611**, 346-355.
5. R. Chang, S. Kim, S. Lee, S. Choi, M. Kim and Y. Park, *Frontiers in Energy Research*, 2017, **5**.
6. D. Winters, K. Boakye and S. Simske, *Sustainability*, 2022, **14**, 4633.
7. M. A. Sabri, S. Al Jitan, D. Bahamon, L. F. Vega and G. Palmisano, *Science of The Total Environment*, 2021, **790**, 148081.
8. J. Ihli, W. C. Wong, E. H. Noel, Y.-Y. Kim, A. N. Kulak, H. K. Christenson, M. J. Duer and F. C. Meldrum, *Nature Communications*, 2014, **5**, 3169.
9. H. Du, M. Steinacher, C. Borca, T. Huthwelker, A. Murello, F. Stellacci and E. Amstad, *Journal of the American Chemical Society*, 2018, **140**, 14289-14299.
10. P. Raiteri and J. D. Gale, *Journal of the American Chemical Society*, 2010, **132**, 17623-17634.
11. A. L. Goodwin, F. M. Michel, B. L. Phillips, D. A. Keen, M. T. Dove and R. J. Reeder, *Chemistry of Materials*, 2010, **22**, 3197-3205.
12. J. W. Singer, A. Ö. Yazaydin, R. J. Kirkpatrick and G. M. Bowers, *Chemistry of Materials*, 2012, **24**, 1828-1836.
13. M. P. Prange, S. T. Mergelsberg and S. N. Kerisit, *Crystal Growth & Design*, 2021, **21**, 2212-2221.
14. F. M. Michel, J. MacDonald, J. Feng, B. L. Phillips, L. Ehm, C. Tarabrella, J. B. Parise and R. J. Reeder, *Chemistry of Materials*, 2008, **20**, 4720-4728.
15. M. P. Schmidt, A. J. Ilott, B. L. Phillips and R. J. Reeder, *Crystal Growth & Design*, 2014, **14**, 938-951.
16. M. Saharay and R. J. Kirkpatrick, *Physical Chemistry Chemical Physics*, 2017, **19**, 29594-29600.
17. A. C. S. Jensen, S. Imberti, S. F. Parker, E. Schneck, Y. Politi, P. Fratzl, L. Bertinetti and W. J. E. M. Habraken, *The Journal of Physical Chemistry C*, 2018, **122**, 3591-3598.
18. S. Leukel, M. Mondeshki and W. Tremel, *Inorganic Chemistry*, 2018, **57**, 11289-11298.
19. S. N. Kerisit, F. N. Smith, S. A. Saslow, M. E. Hoover, A. R. Lawter and N. P. Qafoku, *Environmental Science & Technology*, 2018, **52**, 5902-5910.
20. S. N. Kerisit and M. P. Prange, *ACS Earth and Space Chemistry*, 2019, **3**, 2582-2592.

21. S. A. Saslow, S. N. Kerisit, T. Varga, K. C. Johnson, N. M. Avalos, A. R. Lawter and N. P. Qafoku, *ACS Earth and Space Chemistry*, 2019, **3**, 1624-1630.
22. S. N. Kerisit and M. P. Prange, *Chemical Geology*, 2020, **534**, 119460.
23. J. P. Perdew, K. Burke and M. Ernzerhof, *Phys. Rev. Lett.*, 1996, **77**, 3865-3868.
24. J. P. Perdew, K. Burke and M. Ernzerhof, *Phys. Rev. Lett.*, 1997, **78**, 1396-1396.
25. S. Grimme, *J. Comput. Chem.*, 2006, **27**, 1787-1799.
26. S. Grimme, J. Antony, S. Ehrlich and H. Krieg, *J. Chem. Phys.*, 2010, **132**, 154104.
27. B. Hammer, L. B. Hansen and J. K. Nørskov, *Phys. Rev. B*, 1999, **59**, 7413-7421.
28. Y. Zhang and W. Yang, *Phys. Rev. Lett.*, 1998, **80**, 890-890.
29. J. P. Perdew, A. Ruzsinszky, G. I. Csonka, O. A. Vydrov, G. E. Scuseria, L. A. Constantin, X. Zhou and K. Burke, *Phys. Rev. Lett.*, 2008, **100**, 136406.
30. P. E. Blöchl, *Phys. Rev. B*, 1994, **50**, 17953-17979.
31. G. Kresse and D. Joubert, *Phys. Rev. B*, 1999, **59**, 1758-1775.
32. S. Nosé, *The Journal of Chemical Physics*, 1984, **81**, 511-519.
33. W. G. Hoover, *Physical Review A*, 1985, **31**, 1695-1697.
34. M. Parrinello and A. Rahman, *Journal of Applied Physics*, 1981, **52**, 7182-7190.
35. M. Parrinello and A. Rahman, *Phys. Rev. Lett.*, 1980, **45**, 1196-1199.
36. W. Smith and T. R. Forester, *Journal of Molecular Graphics*, 1996, **14**, 136-141.
37. O. Teleman, B. Jönsson and S. Engström, *Molecular Physics*, 1987, **60**, 193-203.
38. N. H. de Leeuw and S. C. Parker, *The Journal of Chemical Physics*, 2000, **112**, 4326-4333.
39. S. Kerisit and S. C. Parker, *Journal of the American Chemical Society*, 2004, **126**, 10152-10161.
40. N. H. de Leeuw, *The Journal of Physical Chemistry B*, 2002, **106**, 5241-5249.
41. I. P. Swainson, *American Mineralogist*, 2008, **93**, 1014-1018.
42. R. B. Neder and T. Proffen, *J. Appl. Cryst.*, 2020, **53**, 710-721.
43. D. F. Gregory, R. L. Ellis, W. T. B. Kelvin and N. M. Ferrers, *The Cambridge and Dublin Mathematical Journal*, Macmillan, Barclay and Macmillan, 1848.
44. J. W. Gibbs, *Nature*, 1899, **59**, 606-606.
45. A. Hoeher, S. Mergelsberg, O. J. Borkiewicz, P. M. Dove and F. M. Michel, *Acta Crystallographica Section A*, 2019, **75**, 758-765.
46. P. J. Chupas, K. W. Chapman and P. L. Lee, *J. Appl. Cryst.*, 2007, **40**, 463-470.
47. B. H. Toby and R. B. Von Dreele, *J. Appl. Cryst.*, 2013, **46**, 544-549.
48. X. Qiu, J. W. Thompson and S. J. L. Billinge, *J. Appl. Cryst.*, 2004, **37**, 678.
49. H.-W. Wang, L. L. Daemen, M. C. Cheshire, M. K. Kidder, A. G. Stack, L. F. Allard, J. Neuefeind, D. Olds, J. Liu and K. Page, *Chemical Communications*, 2017, **53**, 2942-2945.
50. S. Sen, D. C. Kaseman, B. Colas, D. E. Jacob and S. M. Clark, *Physical Chemistry Chemical Physics*, 2016, **18**, 20330-20337.
51. K. Momma and F. Izumi, *J. Appl. Cryst.*, 2011, **44**, 1272-1276.
52. R. Shannon, *Acta Crystallographica Section A*, 1976, **32**, 751-767.
53. G.-i. Yamamoto, A. Kyono and S. Okada, *Scientific Reports*, 2021, **11**, 22876.
54. A. C. S. Jensen, Dr. rer. nat. Univ.-Diss., Max-Planck-Institut für Kolloid- und Grenzflächenforschung, 2018.
55. M. Albéric, L. Bertinetti, Z. Zou, P. Fratzl, W. Habraken and Y. Politi, *Advanced Science*, 2018, **5**, 1701000.
56. S. E. Wolf, L. Müller, R. Barrea, C. J. Kampf, J. Leiterer, U. Panne, T. Hoffmann, F. Emmerling and W. Tremel, *Nanoscale*, 2011, **3**, 1158-1165.
57. S. Leukel, M. Panthöfer, M. Mondeshki, G. Kieslich, Y. Wu, N. Krautwurst and W. Tremel, *Journal of the American Chemical Society*, 2018, **140**, 14638-14646.
58. M. H. Nielsen, S. Aloni and J. J. De Yoreo, *Science*, 2014, **345**, 1158-1162.
59. Y. G. Bushuev, A. R. Finney and P. M. Rodger, *Crystal Growth & Design*, 2015, **15**, 5269-5279.
60. S. A. Markgraf and R. J. Reeder, *American Mineralogist*, 1985, **70**, 590-600.
61. B. Pokroy, J. S. Fieramosca, R. B. Von Dreele, A. N. Fitch, E. N. Caspi and E. Zolotoyabko, *Chemistry of Materials*, 2007, **19**, 3244-3251.
62. G. Cobourne, G. Mountjoy, J. D. Rodriguez-Blanco, L. G. Benning, A. C. Hannon and J. R. Plaisier, *Journal of Non-Crystalline Solids*, 2014, **401**, 154-158.
63. Y. Shuseki, S. Kohara, K. Ohara, T. Ohkubo, K. Takei, M. G. Tucker, A. I. Kolesnikov, M. T. McDonnell, R. L. Sacci, J. C. Neuefeind and K. Takeuchi, *Journal of the Ceramic Society of Japan*, 2022, **130**, 225-231.
64. J. Bolze, B. Peng, N. Dingenouts, P. Panine, T. Narayanan and M. Ballauff, *Langmuir*, 2002, **18**, 8364-8369.
65. Z. Liu, Z. Zhang, Z. Wang, B. Jin, D. Li, J. Tao, R. Tang and J. J. De Yoreo, *Proceedings of the National Academy of Sciences*, 2020, **117**, 3397-3404.
66. A. C. S. Jensen, S. Imberti, W. J. E. M. Habraken and L. Bertinetti, *The Journal of Physical Chemistry C*, 2020, **124**, 6141-6144.
67. M. Saharay, A. O. Yazaydin and R. J. Kirkpatrick, *The Journal of Physical Chemistry B*, 2013, **117**, 3328-3336.
68. U. R. Kapadi, D. G. Hundiwale, N. B. Patil and M. K. Lande, *Fluid Phase Equilibria*, 2002, **201**, 335-341.
69. R. Innocenti Malini, Y. G. Bushuev, S. A. Hall, C. L. Freeman, P. M. Rodger and J. H. Harding, *CrystEngComm*, 2016, **18**, 92-101.
70. C. E. White, N. J. Henson, L. L. Daemen, M. Hartl and K. Page, *Chemistry of Materials*, 2014, **26**, 2693-2702.
71. Y.-C. Huang, A. Rao, S.-J. Huang, C.-Y. Chang, M. Drechsler, J. Knaus, J. C. C. Chan, P. Raiteri, J. D. Gale and D. Gebauer, *Angewandte Chemie International Edition*, 2021, **60**, 16707-16713.
72. J. Feng, Y. J. Lee, J. D. Kubicki, R. J. Reeder and B. L. Phillips, *Magnetic Resonance in Chemistry*, 2008, **46**, 408-417.
73. H. Nebel, M. Neumann, C. Mayer and M. Epple, *Inorganic Chemistry*, 2008, **47**, 7874-7879.
74. A. C. S. Jensen, I. Rodriguez, W. J. E. M. Habraken, P. Fratzl and L. Bertinetti, *Physical Chemistry Chemical Physics*, 2018, **20**, 19682-19688.

75. P. Opitz, M. P. Asta, A. Fernandez-Martinez, M. Panthöfer, A. Kabelitz, F. Emmerling, M. Mondeshki and W. Tremel, *Crystal Growth & Design*, 2020, **20**, 6831-6846.
76. K. Page, A. G. Stack, S. A. Chen and H.-W. Wang, *Physical Chemistry Chemical Physics*, 2022, **24**, 18340-18346.
77. S. M. Clark, B. Colas, D. E. Jacob, J. C. Neuefeind, H.-W. Wang, K. L. Page, A. K. Soper, P. I. Schodder, P. Duchstein, B. A. Zubiri, T. Yokosawa, V. Pipich, D. Zahn, E. Spiecker and S. E. Wolf, *Scientific Reports*, 2022, **12**, 6870.
78. E. J. Bylaska, M. Valiev, J. R. Rustad and J. H. Weare, *The Journal of Chemical Physics*, 2007, **126**, 104505.
79. H. Du and E. Amstad, *Angewandte Chemie International Edition*, 2020, **59**, 1798-1816.